

## Appendix 1 Workflow of automatic segmentation of vessel lumen

The algorithm for the automatic segmentation of the vessel lumen comprised the following six steps:

(I) Coordinate transformation: each image was transformed from the cartesian coordinate space to the polar coordinate space using Eq. [1] as shown in *Figure S1A*.

$$\begin{cases} x = \rho \cos \theta \\ y = \rho \sin \theta \\ \rho = \sqrt{x^2 + y^2} \\ \tan \theta = \frac{y}{x} \end{cases} \quad [1]$$

(II) Guide wire removal: the threshold method was used to remove the guide wire and catheter artifacts after coordinate transformation. Given that the guide wire was located at the upper edge of the image, it could be removed by setting the gray values to zero according to the corresponding region size as shown in *Figure S1B*.

(III) Catheter artifacts removal: the average gray value of each column was calculated and is displayed in *Figure S1C*. The dark shadow was followed due to the coverage of the catheter artifacts and thus had a low gray value. As *Figure S1D* shows, the minimum of the gray value was obtained, which was 7.5 in this study. The gray value of any column that was smaller than 7.5 was settled to zero. This enabled the catheter artifacts to be removed (*Figure S1E*).

(IV) Morphological operations: after the removal of the guide wire and catheter artifacts, the image was converted into a binary image. The morphological opening method, which was an erosion followed by a dilation, was then applied. The image after the opening operation was reconverted into a grayscale image. *Figure S1F* shows the result of the morphological operations.

(V) Linear interpolation: an obvious feature of the guide wire was that it had a bright reflection, immediately followed by a dark shadow, resulting in the discontinuity of the structures in the segmented image. In the cartesian coordinate space, the contour shape of the vessel was approximately circular. The loop around the center of the transformation was a linear segment after polar coordinate conversion. Therefore, the linear interpolation was applied to make the vessel wall continuous in the current study (*Figure S1G*).

(VI) Coordinate inverse transformation: when the boundary of the region with the guide wire removed was segmented, the complete contour was computed (*Figure S1H*). Then, inverse transformation from the polar coordinate space to the cartesian coordinate space was performed to the segmented contour and the input image was segmented as shown in *Figure S1I*.

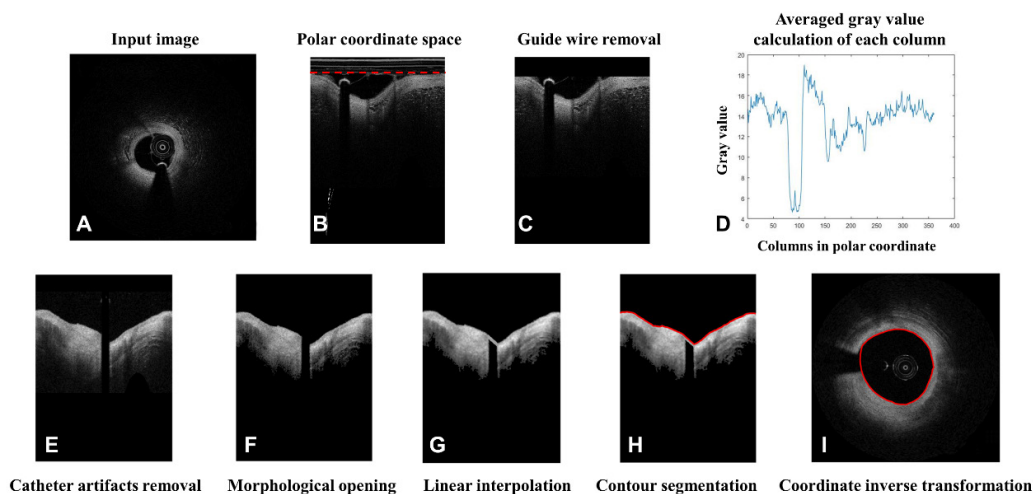


**Figure 1** The workflow of the automatic segmentation algorithm of the vessel lumen (A-I). The red dashed line indicates the positions with gray values of zero. The red line and red circle indicate the boundary of the segmented vessel lumen in the polar coordinate space and cartesian coordinate space, respectively.

## Appendix 2 Co-registration between IV-OCT and 3D angiographic centerline

The 3D centerline was reconstructed via epipolar geometry and the stereo matching algorithm based on 2D angiography. In the current study, at least one DSA image with a visible IV-OCT catheter was chosen to guarantee the coherence of the starting and ending points between DSA and IV-OCT images. It was assumed that the pullback process occurred at a constant speed in this study. The 3D centerline computed from DSA images was exported as discrete points. The segmentations were conducted on IV-OCT images for the region of interest. To ensure more accurate 3D model reconstruction, the interpolation was used to increase the number of slices using the VTK package in Python 3.93 (<https://vtk.org>). The number of discrete points of the 3D angiographic centerline was determined by the final number of slices.

The registration process between the IV-OCT slices and 3D angiographic centerline comprised several sub-steps. First, the scale was converted into millimeter units for the points from the IV-OCT and the angiography to eliminate the resolution difference between the two image modalities. Second, the large side branches in both the DSA and IV-OCT images were identified as the key landmarks. Third, the centroid of each IV-OCT slice was obtained and defined as the midpoint on the perpendicular bisector of the longest line segment between the two points on the lumen contour.

Two coordinate systems were specified:  $xyz$  for the IV-OCT image, and  $x'y'z'$  for the 3D angiographic centerline. The origin of the  $xyz$  coordinate was set as the centroid point of each contour of the IV-OCT slice. Further, the normal vector of the corresponding IV-OCT slice was assigned as  $z$  (0,0,1). The  $x$ -axis was assigned according to the landmarks in the IV-OCT images. It should be noted that the original  $x$  direction was only determined in the slices with key landmarks. In relation to those without identifiable features, the  $x$  direction was assigned depending on the projection of the  $x$  direction decided by the landmarks.

For the space of the 3D angiographic centerline, the local tangent vector of the 3D angiographic centerline was set as the  $z'$ -direction. The key landmarks corresponding to the IV-OCT images were subsequently reconstructed into 3D points in the DSA spatial space via epipolar geometry and the stereo matching algorithm. The reconstructed 3D landmark points were used to determine the original  $x'$  direction. Similar to the IV-OCT coordinate system, the original  $x'$  direction was only determined in the slices with landmarks. In relation to those without identifiable features, the  $x'$  direction was determined depending on the projection of the  $x'$  direction decided by the landmarks. The  $y$ -axis and  $y'$ -axis were accordingly determined after the establishment of the two other axes.

Subsequently, the centroid point of each contour of the corresponding 2D IV-OCT slice corresponded to the points of the 3D angiographic centerline in a one-to-one manner, resulting in the derivation of a translational vector. Two rotations were employed to achieve the transformation from  $xyz$  to  $x'y'z'$ . Specifically, the angle of  $\alpha$  was used to indicate the slope angle between the  $x$ -axis and  $x'$ -axis. The first rotation matrix is shown as Eq. [2]. In fact, the in-plane rotation of each slice was naturally correct when matching each pair of the  $x$ -axis and  $x'$ -axis.

$$TR_1 = \begin{bmatrix} 1 & 0 & 0 \\ 0 & \cos \alpha & -\sin \alpha \\ 0 & \sin \alpha & \cos \alpha \end{bmatrix} \quad [2]$$

Second, the angle of  $\beta$  indicates the slope angle between the  $z$ -axis after the first rotation and the  $z'$ -axis. The second rotation matrix is shown as Eq. [3].

$$TR_2 = \begin{bmatrix} \cos \beta & -\sin \beta & 0 \\ \sin \beta & \cos \beta & 0 \\ 0 & 0 & 1 \end{bmatrix} \quad [3]$$

The IV-OCT slices orthogonal to the 3D angiographic centerline were generated after the translation and rotation. The model was finally exported in triangulation mesh in STL format to facilitate the computational analysis. *Figure S2* shows the co-registration process between IV-OCT and the 3D angiographic centerline.

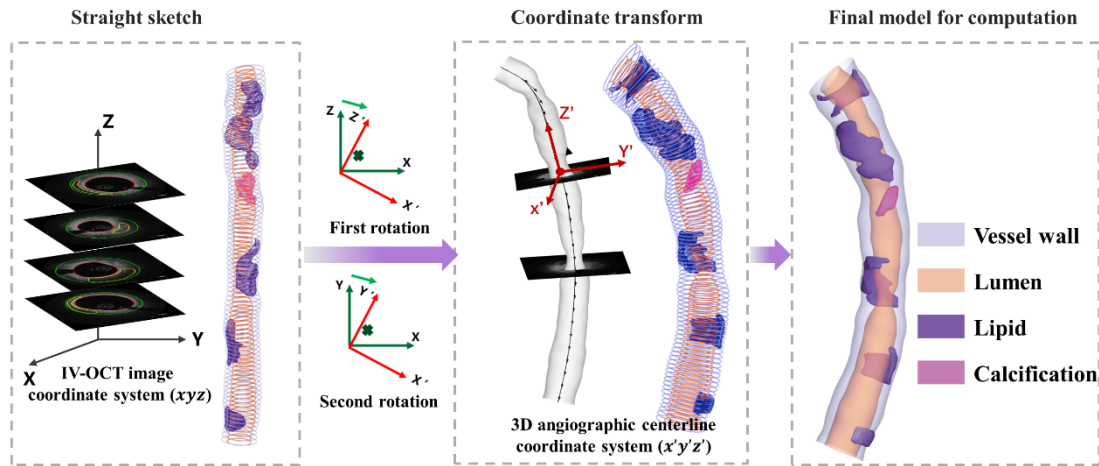


**Figure S2** The registration process between IV-OCT and 3D angiographic centerline. IV-OCT, intravascular optical coherence tomography; 3D, three-dimensional.

### Appendix 3 Boundary condition for 2D FEA (*Figure S3*)

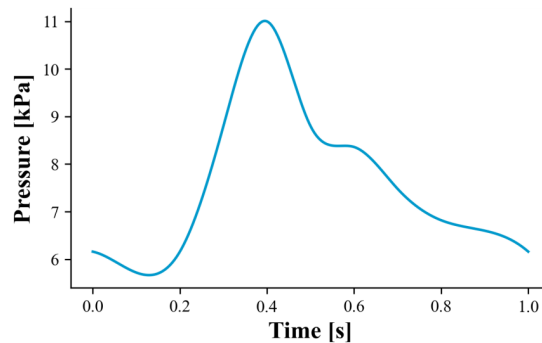


**Figure S3** Pulsatile waveform of pressure for 2D FEA. 2D, two-dimensional; FEA, finite-element analysis.

#### Appendix 4 Settings of constraint and contact

In this study, a four-point constraint was employed for the 2D FEA computation. The four points were determined using the interaction points between the outer vessel wall and the  $x$ -axis and  $y$ -axis as shown in *Figure S4A*. Specifically, the zero-displacement and the zero-rotation in the  $x$  direction were set for two points locating in the  $y$ -direction; while zero-displacement and the zero-rotation in the  $y$ -direction were set for two points locating in the  $x$ -direction. Therefore, these four points only had radial displacement without any tangential displacement. The constraint can guarantee the expansion of the vessel lumen but suppress the rigid translation and rotation. Further, the self-contact interaction was set for the intraluminal surface of the vessel lumen, and the bonded contact was given at the contact region between the vessel wall and the plaque as shown in *Figure S4B*.

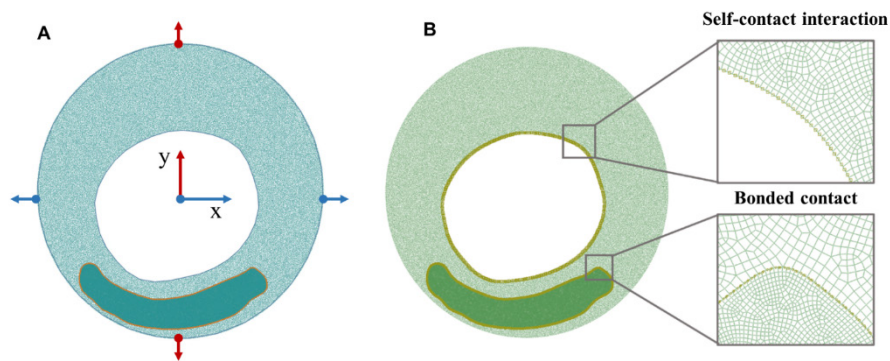


**Figure S4** The constraint and contact settings for the 2D FEA. (A) The four-point constraint. (B) The contact interaction setup. The modification was set to five for enhanced clarity. 2D, two-dimensional; FEA, finite-element analysis.

## Appendix 5 Grid and temporal independence study

To confirm the computational sensitivity to the spatial and temporal resolutions, a grid independence analysis and time-step sensitivity test were conducted on a representative slice. The base grid was 59,714 and the base time step was 0.01 seconds. A finer grid with 105,955 elements and a finer temporal resolution with 0.005 seconds was tested. To quantify the difference, a test point was selected at the thin fibrous cap to investigate the stress difference as shown in *Figure S5*. The average discrepancy of the stress magnitude over one cardiac cycle between the base grid and the finer grid model was 0.63%, while the average difference between the base resolution and the finer resolution was 0.047%. Therefore, the base resolutions with the base time step were considered adequate in the current study.

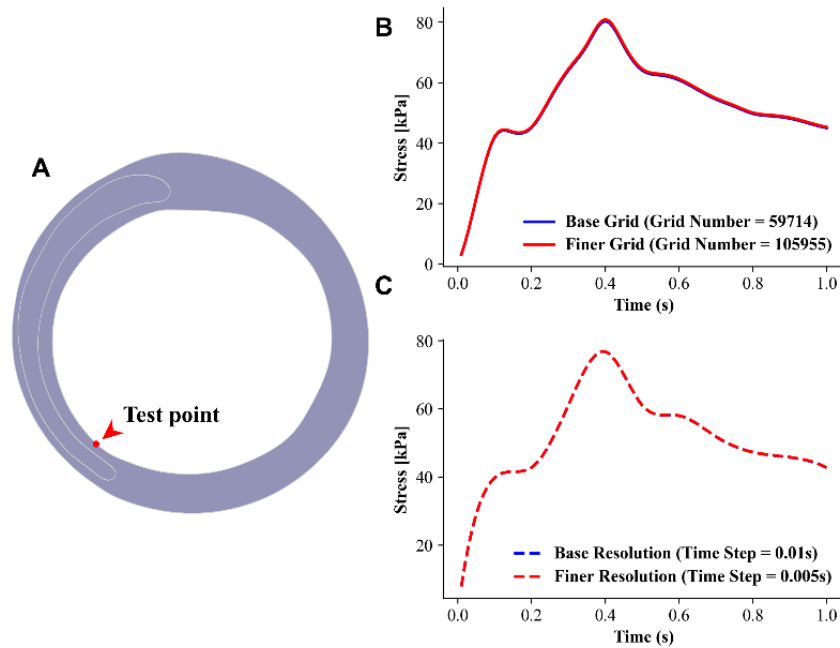


**Figure S5** The grid and temporal independence test with stress. (A) The point on the slice model. (B) The time-variant stress for the base and finer grid model. (C) The time-variant stress for the base and finer resolution model.

## Appendix 6 Mesh independence test for FSI simulation

Before conducting the actual computations, a mesh independent test was performed for both the fluid and solid domains. The base grid for the fluid domain comprised 683,035 elements, while the finer grid comprised 1,522,304 elements. To assess the flow differences, we focused on quantifying the variations in the narrow coronary position, which represented the areas of physiological interest. As *Figure S6A* shows, the WSS exhibited identical variation patterns between the base and fine grid models, with average discrepancies of 0.59%. In relation the solid domain, the number of base grids was 517,987, while the number of finer grids was 1,055,371. The structural stress of the slice in which the plaque was located was extracted and compared between the base grid and finer grid, with mean variations of 4.83% as shown in *Figure S6B*. Therefore, we believed that the base grid resolution was sufficient for this study.

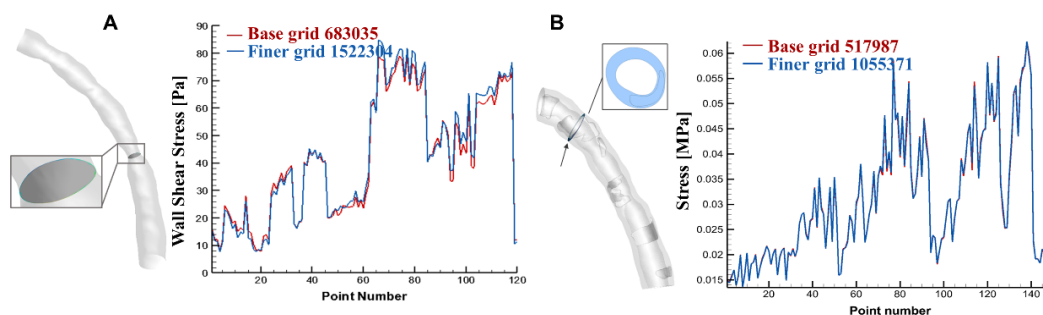


**Figure S6** Mesh independent test. (A) The comparison results of WSS. (B) The comparison results of structural stress. WSS, wall shear stress.

## Appendix 7 Multicollinearity test

A correlation matrix was used to assess the multicollinearity between the 13 candidate factors to choose a regression method to select the key factors. It showed that the degree of correlation between the variables was very high. Thus, the weighted LASSO method was applied for further feature selection as shown in *Figure S7*.

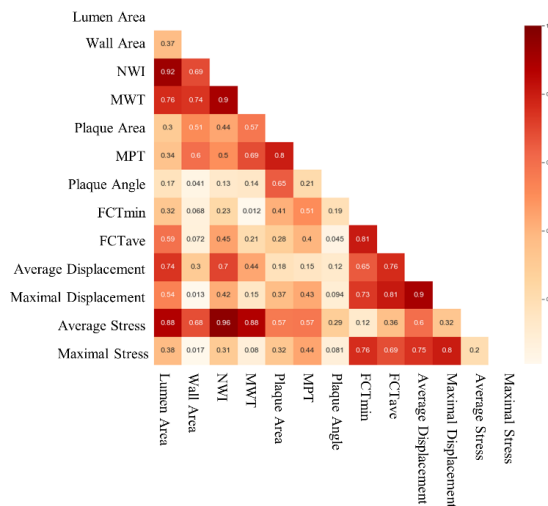


**Figure S7** Correlation matrix of candidate factors. NWI, normalized wall index; MWT, maximal wall thickness; MPT, maximal plaque thickness; FCTmin, minimum fibrous cap thickness; FCTave, average fibrous cap thickness.

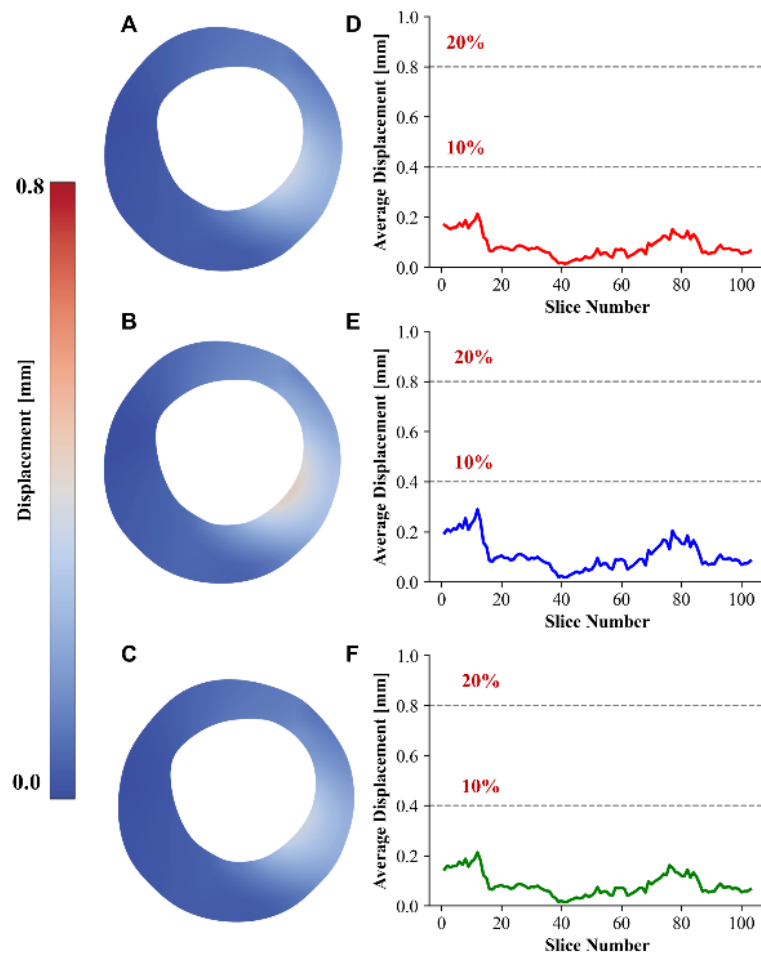
## Appendix 8 Automatic segmentation frameworks for coronary plaque (Table S1)

Table S1 Methods and accuracy for coronary plaque segmentation

Authors	Year	Method	Accuracy
Athanasiou <i>et al.</i> (26)	2014	Image-based method	Calcium: 0.81 Lipid tissue: 0.71 Fibrous tissue: 0.87 Mixed tissue: 0.81
Rico-Jimenez <i>et al.</i> (25)	2016	Linear combination of depth profiles and alternating least square optimization strategy	Overall: 0.85
Kolluru <i>et al.</i> (24)	2018	Convolutional neural network	Calcium: 0.77 Lipid tissue: 0.86 Other: 0.85
Gharaibeh <i>et al.</i> (23)	2019	SegNet	Calcium: 0.76
Lee <i>et al.</i> (22)	2019	Deep learning-based method	Calcium: 0.897 Lipid tissue: 0.827

## Appendix 9 Comparison between 2D FEA and 3D FSI simulations

Figure S8A-S8C show the displacement distributions of one representative vulnerable plaque slice at the early, peak, and late systole, respectively. Further, the average displacement at the early, peak, and late systole of each slice was also computed as shown in Figure S8D-S8F. The average displacement was generally  $<0.2$  mm, approximately 5% of the original dimensions of the considered vessel (4 mm) in the current study. Further, the percentage of nodes with displacement  $>0.8$  mm was also computed at the early, peak, and late systole for each slice. The percentage results were 0, indicating the displacement of all nodes was  $<20\%$ . The results showed the feasibility of employing the linear elasticity material to the vessel wall.



**Figure S8** The displacement patterns at different cardiac moments. (A-C) The displacement distributions at the early, early, peak, and late systole, respectively. (D-F) The average displacement of each slice at the early, early, peak, and late systole, respectively, where 10% and 20% of the initial dimensions are indicated by the gray lines.

## Appendix 10 Comparison between 2D FEA and 3D FSI simulation

The slices were extracted from the FSI simulation results using the IV-OCT slice thickness as the interval to guarantee a good coherence with the 2D FEA results. The maximal stress was subsequently computed and compared for both the FSI slice results and corresponding 2D slices as shown in *Figure S9A*. The 2D finite-element results were generally larger than the 3D FSI results. The difference ratio was computed using Eq. [4], where S indicates the maximal stress. *Figure S9B* shows the difference ratio result, with an average absolute difference of 35.6%.

$$\text{Difference ratio} = \frac{s^{2D} - s^{3D}}{s^{2D}} \times 100\% \quad [4]$$

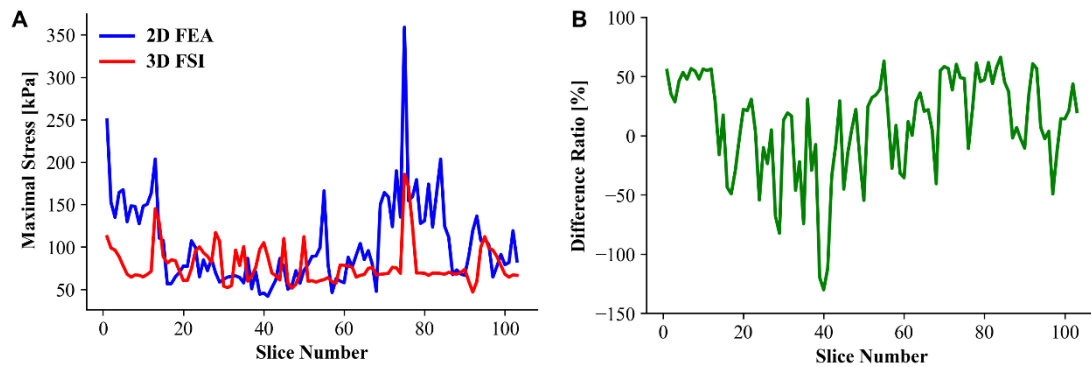


**Figure S9** The comparison of the 2D FEA and 3D FSI simulation results. (A) The difference of maximal stress between the 2D FEA and 3D FSI simulations for each slice. (B) The difference ratio of maximal stress of the 2D FEA results and 3D FSI results for each slice. 2D, two-dimensional; FEA, finite-element analysis; 3D, three-dimensional; FSI, fluid-structure interaction.

## Appendix 11 Comparison between 3D structural computation and FSI simulation

We performed the structural-only simulation and compared the results of the FSI and structural-only computation. The structural-only computation was performed using the same geometry as that of the FSI simulation, and the settings were also the same as those used in the structural analysis of the FSI simulation. For the structural-only results and the FSI results, series slices perpendicular to the 3D angiographic centerline using the IV-OCT slice thickness as the interval were extracted as shown in *Figure S10A,S10B*. Next, the average stress and displacement of each slice were computed and the difference between the structural-only simulation and FSI simulation were also quantified. *Figure S10C,S10D* show the changes in average stress and displacement for each slice. The difference for average stress and displacement was 16.32% and 8.02% between the two methods, respectively. The Bland-Altman plot showed good agreement between the FSI simulation and structural-only simulation for both the average stress and displacement (*Figure S10E,S10F*). Further, the results also showed that the FSI simulation results were generally larger than the structural results.

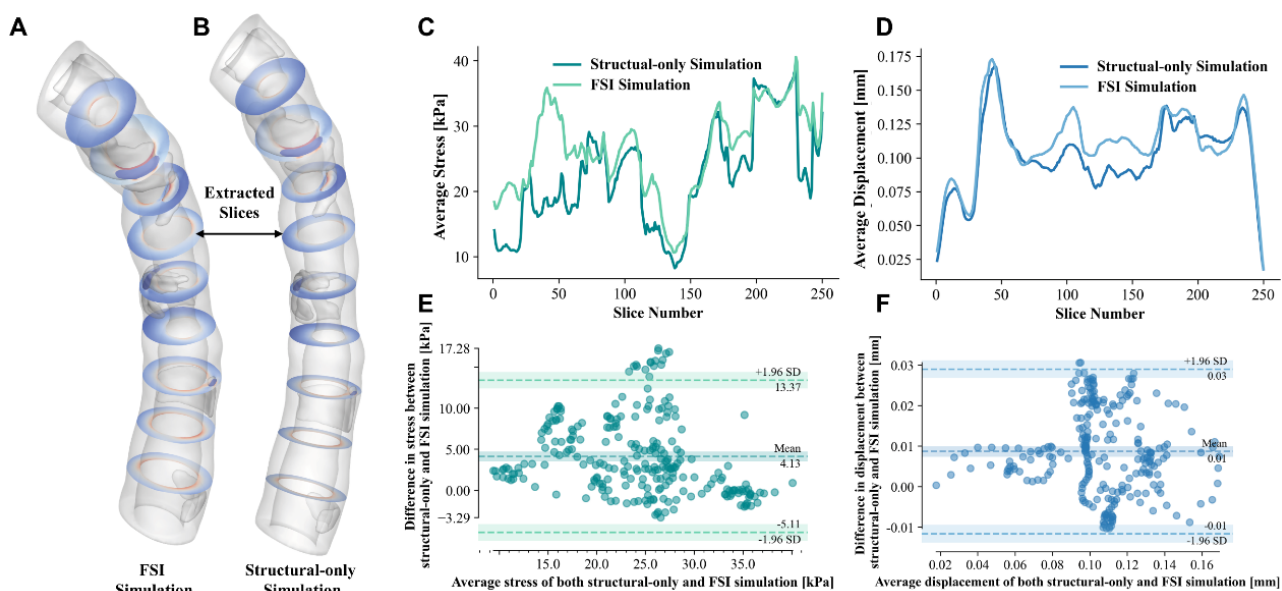


**Figure S10** Comparison of the FSI and structural-only simulation. (A,B) The slice extraction. (C,D) The change of average stress and displacement along the model, respectively. (E,F) Bland-Altman plots for the simulation agreement analysis via stress and displacement, respectively. FSI, fluid-structure interaction.